A Velocity Potential Based Finite State Modeling of Ground Effect

Andro Metry
Graduate Student
Georgia Institute of Technology
Atlanta, GA, USA

J. V. R. Prasad
Professor
Georgia Institute of Technology
Atlanta, GA, USA

David A. Peters
Professor
Washington University
St. Louis, MO, USA

ABSTRACT

A recent development in the Velocity Potential Based Finite State Model (VPBFSM) has introduced an approach to study rotors in ground effect. This approach represents the ground as mass source distributions in the flow field and uses optimization to impose the non-penetration flow boundary condition at the ground. However, it has shown high sensitivity to several parameters, such as the initial guess for optimization and the selection of the ground rotor size. To address these challenges, this paper proposes an alternative approach to impose the flow boundary condition at the ground. The new approach formulates an equation to estimate the strengths of ground mass sources in terms of rotor loading. Additionally, systematic processes are developed to impose the boundary condition for studying an isolated rotor in full, inclined, and partial ground effect cases. This approach is applied to the R-50 helicopter rotor using geometric and aerodynamic data from the literature. The results for the full ground effect show good correlation with the Hayden model and exhibit a rotor inflow trend similar to that of the Pressure Potential Based Finite State Model (PPBFSM). Inclined and partial ground effect cases demonstrate distinct inflow trends compared to the PPBFSM, primarily due to the boundary condition imposed in the current approach, which is not accounted for in the PPBFSM.

NOTATION

a_n^{mc}, a_n^{ms}	Cosine and sine VPBFSM velocity potential states, respectively
C_T	Thrust coefficient $\equiv \frac{T}{\rho\pi\Omega^2 R^4}$
C_L	Roll moment coefficient
C_M	Pitch moment coefficient
$[\hat{D}]$	VPBFSM damping matrix
d	Partial distance from main rotor center to ground plane edge normalized by R
h	Rotor height above ground normalized by R
$[I]$	Identity matrix
i	Imaginary unit
J	Error function
L_k	Sectional lift on the kth blade
$[\hat{L}]$	VPBFSM influence coefficient matrix
$[\hat{M}]$	VPBFSM apparent mass matrix
m, r	Order of associated Legendre function, harmonic
n, j	Degree of associated Legendre function
P_n^m, Q_n^m	Associated Legendre functions
$\bar{P}_n^m, \bar{Q}_n^m$	Normalized associated Legendre functions
R	Rotor radius, ft
r_0	Main rotor radial location
t	Time, second
$[\hat{V}_m]$	Mass flow matrix
$\vec{v}$	Induced velocity vector, nondimensionalized by ΩR
$\vec{v}^*$	Adjoint velocity vector, nondimensionalized by ΩR

Greek

χ	Wake skew angle, rad
$\Delta_n^{mc}, \Delta_n^{ms}$	Cosine and sine costates, respectively
$\nu, \eta, \bar{\psi}$	Ellipsoidal cooridnates
ξ	Streamline coordinate
ρ	Density of air lb/ft^3
ρ_n^m	Normalization factors
τ_n^{mc}, τ_n^{ms}	Cosine and sine pressure coefficients, respectively
Φ_n^m	Pressure potential functions
$\bar{\psi}_k$	Azimuthal coordinate of the kth blade
Ψ_n^m	Velocity potential function
Ω	Rotor rotating speed, rad/s
$\omega_n^{mc}, \omega_n^{ms}$	Cosine and sine pressure coefficients of ground rotor, respectively
$(^*)$	Derivative with respect to nondimensional time, Ωt
$()_{IGE}, ()_{OGE}$	In and out of ground effect, respectively
$()_{main}, ()_{ground}$	Of the main and ground rotor, respectively

INTRODUCTION

The demand for real-time simulation of helicopter flight in ground effect has led to the development of reduced-order models that can accurately capture all physical behaviors while being efficient enough for real-time flight simulation implementation. One of the most well-known models in rotorcraft inflow research is the finite state wake model, which has been developed over the years. Currently, finite state inflow models are widely used in various rotorcraft flight simulation applications due to their low computational effort and ease of implementation. However, these models are somewhat limited when it comes to simulating complex applications involving maneuvering flights near the ground, such as partial, inclined, and dynamic ground effects

When a helicopter flies near ship decks, the ground, or the summits of buildings, it encounters different phenomena such as full, inclined, or partial ground effect. Thus, no flux through these surfaces in the flow field should be the boundary condition. Moreover, for a rotor flying near the ground at a constant power consumption, the thrust generated by the rotor increases as the airflow through the rotor decreases due to the ground effect.

Many studies have been conducted to understand and simulate the different types of ground effect. The most popular models include the image rotor and pressure potential in the flow field using finite state wake model (Refs. 1–5). The image rotor model can automatically satisfy the non-penetration flow boundary condition at the ground surface. This is achieved by using the ground as a mirror to create an image rotor below the ground, which cancels out the mutual interaction in terms of normal flow at the ground plane with the actual rotor above the ground. However, this method fails to accurately represent inclined ground, moving ground, or partial ground effect. A few studies (Refs. 1–5), in the past have modeled various cases of ground effect including full, inclined, and partial using a source-like spatially distributed pressure perturbation over the footprint of the rotor, called the 'ground rotor', at the ground plane. This contribution of the ground is added to the pressure perturbation of the main rotor to obtain the total pressure perturbation at the rotor disk, which is then used to determine the rotor inflow in-ground effect. These attempts showed good correlations with experimental data for steady ground effect cases. However, they could not model dynamic ground effect, as the state-of-the-art finite state inflow modeling at that time did not allow for explicit modeling of induced velocities inside the rotor wake.

Using a velocity potential representation of the flow field, Morillo and Peters (Ref. 6), and Peters et al. (Ref. 7) developed the three-dimensional finite state model by applying the Galerkin approach, which allowed for computing flow velocities at any point within the rotor wake above and on the rotor disk. Yu and Peters (Refs. 8–10) used the velocity potential-based finite state inflow modeling from Refs. (6, 7) along with the concept of a 'ground rotor' pressure field from Refs. (1–5) to model various ground effect cases, including normal, partial, and dynamic. Additionally, Yu and Peters in Ref. (10) used a mass source distribution at the 'ground rotor' with an exit pressure equal to that exerted by the rotor at the ground plane, which showed good correlation with experimental data for various steady ground effect cases. Furthermore, they showed that a quasi-steady ground effect modeling of dynamic ground effect would give rise to significant error. Unlike the image rotor approach, the 'ground' rotor pressure field approach pursued in Refs. (1–5, 10) does not explicitly account for the 'non-penetration of flow at the ground' boundary condition.

Moreover, Metry, Prasad, and Peters in Ref. (11) have developed a new model where the ground is represented as mass source distributions in the flow field and satisfies the non-penetration flow boundary condition at the ground plane. As such, the ground rotor is represented as a region much larger than the main rotor, and the mass sources are distributed at the ground rotor where the boundary condition is enforced within the main rotor wake radius. The model development pursued in Ref. (11) makes use of the velocity potential-based finite state modeling for single rotors (Refs. 6, 7), ground effect modeling (Refs. 8–10), and coaxial rotors (Refs. 12, 13), where the lower rotor is treated as a non-lifting rotor with mass source distributions of unknown strengths. Additionally, the size of the lower rotor is considered unknown and is determined from the non-penetration flow boundary condition. Thus, the model is formulated to compute the strength of the unknown mass source distributions and the size of the non-lifting ground rotor using an optimization method to enforce the non-penetration flow boundary condition at the ground plane. Although the model of Ref. (11) showed good correlation with the Hayden model and Pressure Potential Based Finite State Model (PPBFSM), it had to deal with several challenges. For instance, the approach is highly sensitive to parameters such as the initial guess of ground source distribution strengths for optimization, the number of mass source distributions, the number and location of collocation points at the ground plane, and the choice of ground rotor size. These sensitivities introduce uncertainty into the approach. Therefore, a new approach is necessary to mitigate these challenges.

The primary objective of this study is to develop an alternative approach for imposing the boundary condition at the ground without relying on an optimization method. To achieve this, an equation has been formulated to estimate the strengths of the ground mass source distributions in terms of the main rotor loading. However, this equation fails to enforce the boundary condition at the ground due to the exclusion of the $n = m$ terms in computing the ground flow velocities, which would otherwise introduce infinite kinetic energy into the flow field, as discussed in Ref.(10). Consequently, methods have been developed to adjust the estimated strengths of the mass source distributions and the ground rotor size to properly impose the boundary condition at the ground and analyze the behavior of the R-50 unmanned helicopter rotor in normal, inclined, and partial ground effect cases. The results of the full ground effect case have been compared with the Hayden model and PPBFSM, while the results of the inclined and partial ground effect cases have been correlated with PPBFSM.

The paper is structured as follows: First, the formulation of the Velocity Potential Based Finite State Model (VPBFSM) for a dual-rotor system is presented, which is used to study an isolated rotor in various ground effect cases. This is followed by a description of the systematic processes developed to impose the boundary condition at the ground for full, inclined, and partial ground effect cases. The approach is then applied to the R-50 helicopter rotor in steady-state conditions for these ground effect cases. The paper concludes with a summary of key findings and recommendations for future research.

VELOCITY POTENTIAL BASED FINITE STATE MODEL

A detailed derivation for multi-rotor using VPBFSM is presented in Refs. (12, 13). Thus, the derivation of this model is not attempted in this study. Instead, some review and modifications are included for the dual rotor velocity potential model to arrive at a single rotor and ground rotor. Also, the assumptions that have been made in Refs. (12, 13) are still used in this model. They are as follows: the flow around the rotor disk is incompressible, inviscid, and uses a rigid cylindrical wake geometry.

Dual-Rotor Velocity Potential Based Finite State Model (VPBFSM)

The governing equation of VPBFSM for the dual rotor is as follows:

$$[M]^{+}\begin{Bmatrix} {a_1}^{*} \\ {\Delta_1}^{*} \\ {a_2}^{*} \end{Bmatrix} + [\hat{D}][\hat{V}_m][\hat{L}]^{-1}[\hat{M}]\begin{Bmatrix} a_1 \\ \Delta_1 \\ a_2 \end{Bmatrix} = [\hat{D}]\begin{Bmatrix} \tau_1 \\ \tau_1^{*} \\ \tau_2 \end{Bmatrix} \tag{1}$$

where

$[\hat{M}]^{+} = diag([\tilde{M}], -[\tilde{M}], [\tilde{M}])$

$[\hat{M}] = diag([\tilde{M}], [\tilde{M}], [\tilde{M}])$

$[\hat{D}] = diag([\tilde{D}], [\tilde{D}], [\tilde{D}])$

$[\hat{V_m}] = diag([\tilde{V_m}], [\tilde{V_m}], [\tilde{V_m}])$

$[\hat{L}] = diag([\tilde{L}(\tilde{X_1})], [\tilde{L}(\tilde{X_2})], [\tilde{L}(\tilde{X_2})])$

$\hat{X_1} = tan(\tilde{X_1}/2), \;\; \hat{X_2} = tan(\tilde{X_2}/2)$

In Eq. (1), $\{a\}$ and $\{\Delta\}$ are vectors of velocity potential states and costates, respectively. Hence, adding the costate variable to compute the flow below the rotor as the state variable can be used in calculating on and above the rotor disk. The adjoint equation of costates must be integrated backward in time as forward time-marching will make the system unstable due to the appearance of a negative sign attached to the derivative term; The detail of this method is mentioned in Ref. (12). Also, $\{\tau\}$ is a column vector consisting of pressure coefficients corresponding to load distribution or mass sources distributions; It is interesting to note that τ_n^m with $n+m = odd$ corresponds to pressure discontinuities while $n+m = even$ correspond to mass sources terms (injection of flow into the flow field). $[\hat{M}]$, $[\hat{D}]$, $[\hat{V}_m]$, and $[\hat{L}]$ are apparent mass, damping, mass flow parameter and inflow influence coefficient matrices. These matrices are block diagonal and have analytical expressions similar to single rotor velocity potential finite state model except $[\hat{V}_m]$ which is discussed in detail in Ref. (12). Note that $\{\tau^{*} = (-1)^{j+1}\tau\}$, where j is the index of the radial distribution.

The pressure coefficients used in Eq. (1) can be computed using the following equation:

$$\tau_n^{0c} = \frac{1}{4\pi}\sum_{q=1}^{Q}\int_0^1 \frac{L_q}{\rho\Omega^2R^3}\Psi_n^0(\bar{r})d\bar{r}$$

$$\tau_n^{mc} = \frac{1}{2\pi}\sum\nolimits_{q=1}^{Q}\int_0^1 \frac{L_q}{\rho\Omega^2R^3}\Psi_n^0(\bar{r})d\bar{r}cos(m\psi_q) \tag{2}$$

$$\tau_n^{ms} = \frac{1}{2\pi}\sum_{q=1}^{Q}\int_0^1 \frac{L_q}{\rho\Omega^2R^3}\Psi_n^0(\bar{r})d\bar{r}sin(m\psi_q)$$

where L_q represents the sectional lift of qth blade, Q is the total blade number, R is the rotor radius, ρ is the density, Ω is the rotor rotational speed, $\bar{r}$ is the non-dimensional radial blade coordinate, ψ_q is the azimuthal angle of qth blade, and Ψ_n^m is the radial shaping function which has analytical formulation provided in Ref. (14). Note that uniform inflow (τ_1^{0c}), fore-to-aft (τ_2^{1c}), and side-to-side (τ_2^{1s}) pressure coefficients are directly related to rotor thrust (C_T), aerodynamic pitch moment (C_M), and roll moment (C_L) coefficients, respectively.

VPBFSM Modification for Steady State and Ground Effect

Additional assumptions have been made to the governing equation (Eq. 1) to study an isolated rotor in ground effect. First, the time-dependent term in the governing equation is removed as this paper focuses on the steady-state flow case. Second, the rotor is in hover so the $[L]^{-1}[\tilde{M}]$ results in identity matrix $[I]$. Finally, to distinguish between pressure coefficient due to load distributions and mass source distributions, (ω) will be used instead of (τ_2) to represent the mass source distributions at the ground rotor. In other words, the main rotor and ground rotor (dual-rotor) are represented by load distributions (τ_1) and mass source distributions (ω), respectively. Also, the velocity states of the ground will be represented as c instead of a_2

Thus, Eq. (1) is modified and the final governing equation is as follows:

$$[\hat{V}_m]\begin{Bmatrix} a_1 \\ \Delta_1 \\ c \end{Bmatrix} = \begin{Bmatrix} \tau_1 \\ \tau_1^{*} \\ \omega \end{Bmatrix} \tag{3}$$

where $\hat{V}_m$ is the mass flow parameter and can be simplified for axial and steady flow (Ref. 10) and defined as follows:

$$\hat{V}_m = \begin{bmatrix} V & & & 0 \\ & 2V & & \\ & & \ddots & \\ 0 & & & 2V \end{bmatrix} \quad , where \quad V = \sqrt{\frac{C_T}{2}} \tag{4}$$

After obtaining the states and co-states, the velocities can be computed; Two types of velocities for each rotor. For instance, the main rotor will have a self-induced (self-flow) velocity and flow velocity of the main rotor on the ground. As discussed in Ref. (6), the on and above rotor-induced flow velocity is computed using a velocity potential relationship which is expanded in the ellipsoidal domain (see Appendix A) by employing the first and second kinds of the Legendre functions, as shown in Eqs. (5 and 6).

$$\vec{v} = \sum_{m=0}^{\infty} \sum_{n}^{\infty} (a_n^{mc} \Phi_n^{mc} + a_n^{ms} \Phi_n^{ms}) \tag{5}$$

$$\begin{Bmatrix} \Phi_n^{mc} = \bar{P}_n^m \bar{Q}_n^m cos(m\bar{\psi}) \\ \Phi_n^{ms} = \bar{P}_n^m \bar{Q}_n^m sin(m\bar{\psi}) \end{Bmatrix} \tag{6}$$

where $\vec{v}$ is the flow-induced velocity on or above a rotor which can be used for the main rotor or the ground rotor. $\bar{P}_n^m$, and $\bar{Q}_n^m$ are the first and secondary normalized associated Legendre functions (see Appendix B), respectively. The difference between the main rotor and the ground rotor in using Eq. (5) would be identifying n in the second summation of this equation; for the rotor, $n = m+1$, and for the ground, $n = m+2$. Hence, n = m terms cannot be used because using them would introduce infinite kinetic energy into the flow field, as discussed in Ref. (8).

Furthermore, to calculate the induced velocity below the rotor, an adjoint theorem has been developed and the detailed derivation of this theorem is discussed in Refs. (12, 15). For steady-state case, the adjoint theorem can be modified from the developed equation mentioned in Refs. (12,15) by removing the time-dependent term. Figure 1 shows how to compute the induced velocity below the disk using the coordinate system displayed in this figure. For instance, induced velocity at point A ($\vec{v}_A$) can be calculated using the velocity at point B ($\vec{v}_B$), and the adjoint velocities at points C ($\vec{v}_C^*$) and D ($\vec{v}_D^*$), and can be defined as:

$$\vec{v}_A(r_0, \tilde{\psi}_0, \tilde{\xi}_0) = \vec{v}_B(r_0, \tilde{\psi}_0, 0) + \vec{v}_c^*(r_0, \tilde{\psi}_0, 0) - \vec{v}_D^*(r_0, \tilde{\psi}_0, -\tilde{\xi}_0) \tag{7}$$

It should be noted that since Eq. (7) ignores the time-dependent variable, there is no need for time marching backward to obtain the costate and then compute the ($\vec{v}_C^*$) as mentioned in Ref. (12). This is because the costate will be equal to the state, and this means that $\vec{v}_C^* = \vec{v}_B$. This is also one of the reasons that the system in Eq. (1) can be decoupled to arrive at Eq. (3).

METHODOLOGY FOR GROUND EFFECT MODEL

After modifying the governing equation of the dual-rotor Velocity Potential Based Finite State Model (VPBFSM) to study an isolated rotor in various types of steady ground effect cases, this section will detail the processes of imposing the non-penetration flow boundary condition for full, inclined, and partial ground effect cases. A critical requirement for this

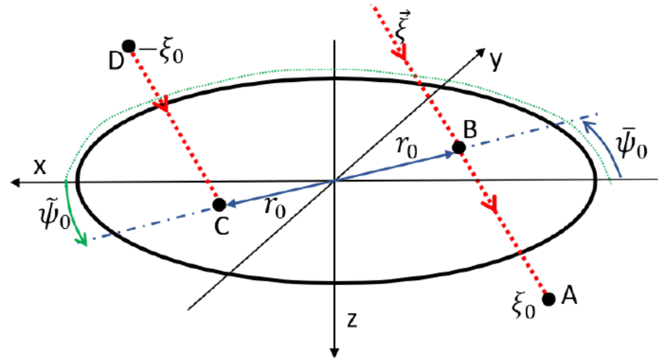

Figure 1: Coordinate system for computing induced velocity below the rotor, (Ref. 13).

process is determining the strengths of the mass source distributions, which are necessary to satisfy the boundary condition and solve the governing equation (Eq. 3). In this paper, an equation is developed to estimate the strengths of the mass source distributions in terms of rotor loading. This is achieved by equating the main rotor wake velocity at the ground, produced by the rotor loading, with the velocity of the flow exiting the mass source distributions at the ground. The developed equation is as follows:

$$\begin{gathered} \omega_j^r = [S_{jn}^{rm}]\ \tau_n^m \\ r = 0,1,\ldots \quad j = r+2, r+4, \ldots \\ m = 0,1,\ldots \quad n = m+1, m+3, \ldots \end{gathered} \tag{8}$$

where $[S_{jn}^{rm}]$ is a correlation matrix. For details on computing this correlation matrix and deriving Eq. (8), see Appendices C and D. It is important to note that the $n = m$ ($r = j$) mass source terms have been excluded in this study since these terms introduce infinite kinetic energy into the flow field, as discussed in Ref. (10). Excluding these terms prevents the imposition of non-penetration flow boundary condition at the ground plane. To address this challenge in studying full, inclined, and partial ground effect cases, a specific systematic process has been developed for each case. Each process adjusts the estimated mass source distributions and the size of the ground rotor to enforce the non-penetration flow boundary condition at the ground.

Full Ground Effect Methodology

Figure 2 shows the schematic for modeling a hovering rotor in full ground effect. A process has been developed to impose the non-penetration flow boundary condition at the ground. This is achieved by adjusting the estimated mass source strengths and the ground rotor size. The process is as follows:

1. Estimate the mass source strengths for the ground rotor using Eq. (8) and a ground rotor of the same size as the main rotor.

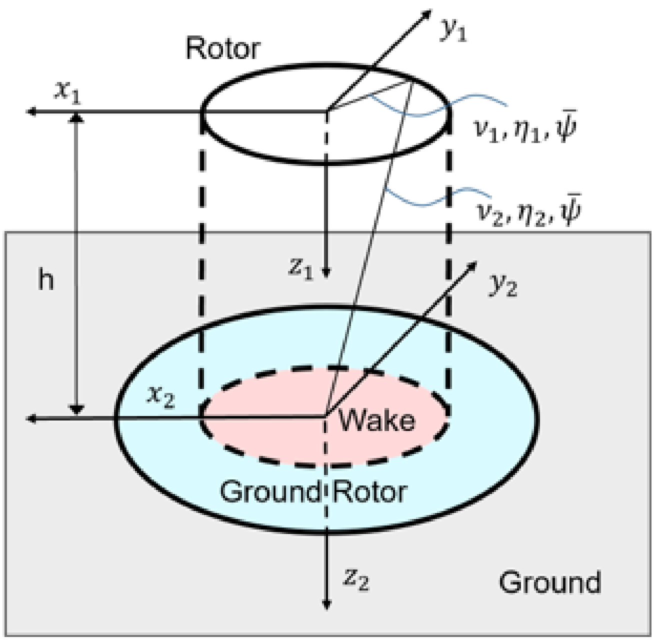

Figure 2: Schematic for modeling of hovering rotor in full ground effect.

2. Change the sign of all estimated mass source strengths computed for the ground rotor to positive values, except for ω_2^0, which should remain unchanged as computed (a negative value).
3. Adjust ω_2^0 until the center of the boundary condition curve reaches a zero flow velocity value.
4. Vary the ground rotor size to be larger than the main rotor size until the non-penetration flow boundary condition is met within the main rotor wake radius.

In applying the last step, the ground rotor size is chosen to achieve a low standard relative error and a low error in percent using all collocation points (zero flow velocity points) within 40% of the rotor wake radius at the ground. As mentioned in Ref. (11), imposing the non-penetration flow boundary condition at all collocation points within 40% of the rotor wake radius at the ground is sufficient. In other words, the low standard relative error condition is used to ensure that the rotor inflow distribution provides an average rotor inflow comparable to the Hayden model. The low error in percent within 40% of the rotor wake radius at the ground is used to guide the solution in finding the ground rotor size that meets the flow boundary condition.

Moreover, the ground effect factor (K_G) is defined as the ratio of the average rotor inflow in ground effect (IGE) and out-of-ground effect (OGE), i.e.,

$$K_{G_{FiniteState}} = \frac{V_{IGE}}{V_{OGE}} \tag{9}$$

As such, the following standard relative error is used in selecting the ground rotor size:

$$\text{Standard relative error } = |K_{G_{FiniteState}} - K_{G_{Hayden}}| \tag{10}$$

where $K_{G_{Hayden}}$, taken from Ref. (16) for the Hayden model, is:

$$K_{G_{Hayden}} = \frac{1}{0.9926 + 0.03794(2/h)^2} \tag{11}$$

The error in percent, defined in (Ref. 11), is as follows:

$$J = \frac{\sqrt{\sum_{j=1}^{nc} (V_{z_{ground_j}})^2}}{2\, V_{z,aveRotor}} X100 \tag{12}$$

Where J is Error in percent, $V_{z_{ground}}$ is the total axial velocity at the ground, $V_{z,aveRotor}$ is the rotor average induced velocity, and nc is the number of collocation points used to impose the non-penetration flow boundary condition at the ground.

Inclined Ground Effect Methodology

Figure 3 shows the schematic for modeling a hovering rotor in inclined ground effect. The coordinate system described in Ref. (3) can be used to study an isolated rotor above inclined ground. However, in this study, a simpler coordinate system is adopted to calculate the following velocities: the flow velocity of the main rotor on the ground, the self-flow velocity of the main rotor, the self-flow velocity of the ground rotor, and the flow velocity of the ground rotor on the main rotor.

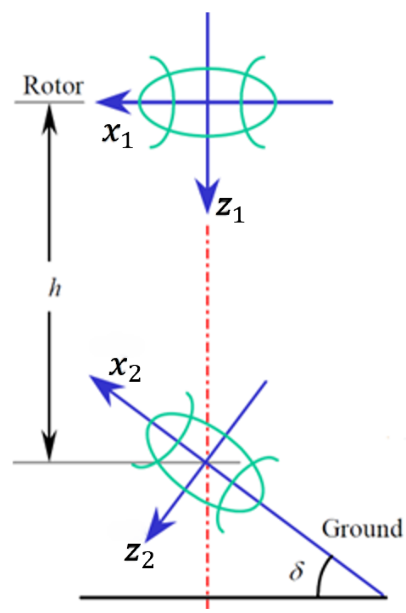

Figure 3: Schematic for modeling of hovering rotor in inclined ground effect.

Both the self-flow velocities of the main and ground rotors are computed using the same coordinate system as in the full ground effect case since each rotor operates within its frame of reference. To accurately account for the interaction between the main rotor and the ground rotor, the coordinate system is adjusted to consider the inclination of the ground along the z-axis. This adjustment ensures that the z-axis of the wake remains vertical, even when the ground plane is inclined. This adjustment is expressed as

$$z = x\,tan(\delta) + h \tag{13}$$

where z is the $z-coordinate$ of point D (see Fig. 1), h denotes the non-dimensional rotor height above the ground, x represents the $x-axis$ coordinate of point D, and δ is the inclination angle of the ground.

Moreover, the total flow velocity of the main rotor is determined by combining its self-flow velocity with the flow velocity of the ground rotor on the main rotor. Similarly, the total flow velocity of the inclined ground is calculated by adding the self-flow velocity of the ground rotor to the product of the cosine of the inclination angle and the flow velocity of the main rotor on the ground.

Furthermore, a process has been developed to adjust the estimated strengths of the mass source distribution over the inclined ground and ground rotor size to impose the non-penetration flow boundary condition on the inclined ground. The process is as follows:

1. Estimate the mass source strengths for the inclined ground rotor using Eq. (8) and a ground rotor of the same size as the main rotor.

2. Change the sign of all estimated mass source strengths computed for the ground rotor to positive values, except for ω_2^0, which should remain unchanged as computed (a negative value).

3. Use the ground rotor radius equivalent to the one determined for this rotor height above the ground, as established in the full ground effect case.

4. Adjust the value of ω_2^0 until the lowest point of the boundary condition curve (total flow velocity at the ground) reaches zero flow velocity. Note that, the boundary condition is imposed within the rotor wake radius at the ground.

Partial Ground Effect Methodology

The tandem concept (Ref. 12), which involves an upper and lower rotor with an offset distance between them, is applied to analyze the partial ground effect case. In this configuration, both rotors typically generate lift. However, for the partial ground effect case, the lower rotor is treated as a non-lifting surface representing the ground by replacing its lifting characteristics with distributions of mass sources. The mass source strengths for the ground rotor are initially estimated using a rotor of the same size as the main rotor. These estimated strengths are then distributed over a larger radius and adjusted to effectively impose the boundary condition. This boundary condition is applied within the overlap region between the main rotor and the ground rotor, as shown in Fig. 4.

Moreover, nine mass source distributions are used to impose the boundary condition at the ground: five zero harmonics

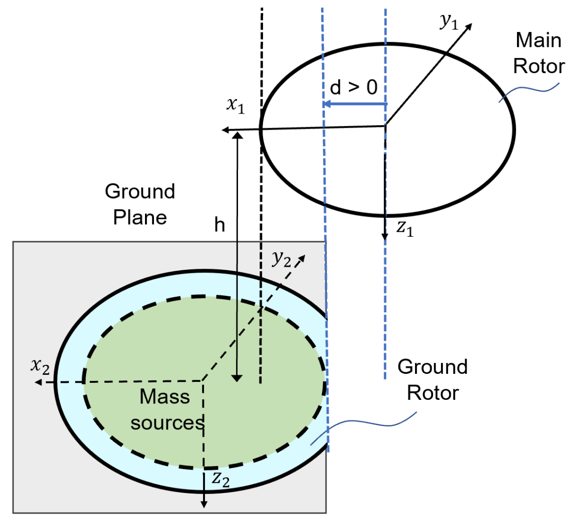

(a) Main rotor center is outside the ground plane

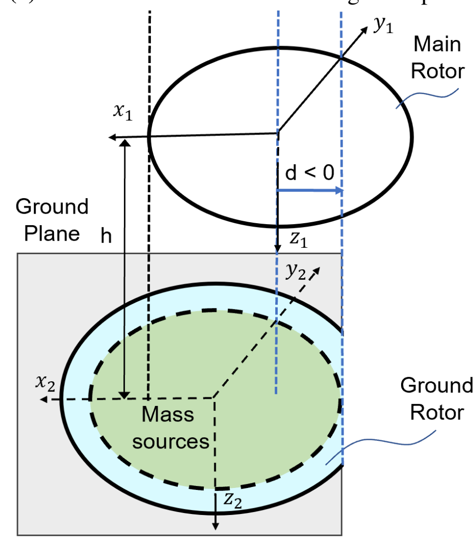

(b) Main rotor center is inside the ground plane

Figure 4: Schematic for modeling of hovering rotor in partial ground effect.

and four first harmonics. Five zero harmonics are employed because Ref. (11) indicates that, for the full ground effect case, five zero harmonics are sufficient to satisfy the boundary condition. First harmonics are used to account for the non-axisymmetric nature of rotor inflow, with four terms selected based on the table of even and odd terms discussed in Ref. (6).

Additionally, four main cases are used to represent all types of partial ground effect, where d denotes the distance from the center of the main rotor to the edge of the ground plane, as shown in Fig. 4:

- Case 1: $d \geq 1$, out-of-ground effect case. Note that the d range shown in this study is in the main rotor frame of reference.

- Case 2: $d \leq$ -1, full ground effect case.

- Case 3: $0 \leq d < 1$, the main rotor footprint center is outside the ground plane, as shown in Fig. 4a.

- Case 4: $-1 < d < 0$, the main rotor footprint center is inside the ground plane, as shown in Fig. 4b.

To impose the non-penetration flow boundary condition at the ground using nine mass source distribution terms, the following procedure is used for these four partial ground effect cases:

- Case 1: No adjustment to the mass source terms is required as it is the out-of-ground effect case, and the strengths of the mass source distributions are zero in this case.

- Case 2: Follow the detailed steps discussed in the full ground effect methodology section .

- Case 3: Require the following steps to satisfy the non-penetration flow boundary condition at the partial ground rotor:

    1. Estimate the mass source strengths for the ground rotor using Eq. (8) and a ground rotor of the same size as the main rotor.

    2. Change the sign of all estimated mass source strengths computed for the ground rotor to positive values, except for ω_2^0, which should remain unchanged as computed (a negative value).

    3. Use the ground rotor radius equivalent to the one determined for this rotor height above the ground, as established in the full ground effect case. Note that the ground is partial as shown in Fig. 4a. The green region in the figure, with a dashed contour, corresponds to the ground area of the same size as the main rotor, and its effect is considered on the main rotor.

    4. Adjust the value of ω_2^0 until the lowest point of the boundary condition curve (total flow velocity at the ground) reaches zero flow velocity.

    5. Adjust ω_3^1 such that the boundary condition curve is nearly flattened.

    6. Modify ω_5^1 to align the nearly flattened section of the boundary condition curve to zero flow velocity line. Hence, ω_5^1 will be a negative value to move the boundary condition curve to the zero flow velocity line.

- Case 4: Use the first four steps from case 3; additionally, it requires the following steps to meet the non-penetration flow boundary condition at the partial ground:

    1. Adjust ω_7^1 such that the boundary condition curve is nearly flattened.

    2. Modify ω_5^1 to align the nearly flattened section of the boundary condition curve to zero flow velocity. Hence, the ω_5^1 will be a negative value to move the boundary condition curve to the zero flow velocity line.

    3. Change ω_3^1 such that the aft section of the total main rotor inflow is close to the out-of-ground effect case.

    4. Revise ω_2^0 to align the total rotor inflow curve close to the full-ground effect result of this rotor height above the ground.

    5. Repeat steps 1 and 2 of adjusting ω_7^1, and ω_5^1 until the boundary condition is met at several collocation points (zero flow velocity points) are achieved.

The steps outlined above for Cases 3 and 4 are developed to ensure that the non-penetration flow boundary condition is satisfied within the overlap region. The adjustments involve modifying the strengths of ω_2^0, ω_3^1, ω_5^1, and ω_7^1. Notably, ω_2^0 and ω_3^1 influence both the total rotor inflow curve and the total ground flow velocity (boundary condition) curve. In contrast, ω_5^1 and ω_7^1 primarily affect the boundary condition curve with minimal impact on the total rotor inflow curve.

RESULTS AND DISCUSSION

In the present study, two assumed load distributions (τ_1^0, τ_3^0) are used to study an isolated rotor in full, inclined, and partial ground effect. Figure 5 displays the assumed load distributions for the R-50 unmanned helicopter rotor with a thrust coefficient of 0.004; This rotor data is shown in Table 1.

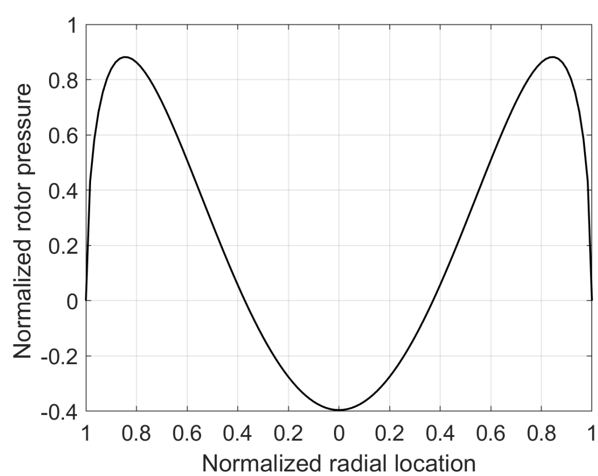

Figure 5: Assumed rotor radial load distribution.

Moreover, the first load distribution (τ_1^0) is defined as follows:

$$\tau_1^0 = \frac{\sqrt{3}C_T}{4} \tag{14}$$

Table 1: R-50 Helicopter Rotor Parameters.

Rotor diameter	3.07 m
Blade chord	0.106 m
Gross weight	522 N
Airfoil	DAE 41
Built-in twist	-3.5°
Rotor solidity	0.044
Rotational speed	78.5 ± 1.3 rad/sec
Tip Mach No.	0.36
Re. at 75 % radius station	6.50 x 10^5

The second load distribution (τ_3^0) is computed in terms of τ_1^0 as shown in Eq. (15).

$$\tau_1^0 = -\tau_3^0 \tag{15}$$

Furthermore, a preliminary result is shown in Fig. 6 for the full ground effect case using 10 mass source distributions, with $R_{ground} = R_{main}$, and the rotor is at a non-dimensional height above the ground of $h = 1.0$.

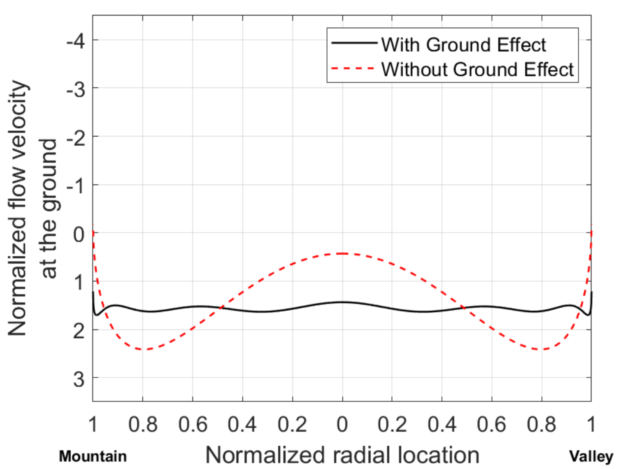

Figure 6: Boundary condition for $H = R_{main}$, and $R_{ground} = R_{main}$ case.

This plot shows the case of using the estimated strengths of the mass source distributions (Eq. 8) without adjustment to the strengths or the ground rotor size. The black solid curve in this plot represents the total flow velocity at the ground (boundary condition curve), and the red-dashed curve corresponds to the main rotor wake velocity at the ground. This figure shows that the boundary condition is not satisfied, as the total flow velocity at the ground is positive, indicating flow through the ground. The reason for not meeting the boundary condition at the ground using the estimated strengths (Eq. 8) is due to the exclusion of the $n = m$ terms in computing the ground flow velocities; Ref. (10) illustrated that using these terms would introduce infinite kinetic energy in the flow field. Thus, to satisfy the boundary condition at the ground, methods of adjusting the mass source distributions and ground rotor size are developed for full, inclined, and partial ground effect cases in the methodology section.

Isolated Rotor in Full Ground Effect

Five mass source distributions are used to impose the boundary condition at the ground within the main rotor wake radius for an isolated rotor in full ground effect. As demonstrated in Ref. (11), these distributions are sufficient to satisfy the ground boundary condition. Figure 7 illustrates the case where $h = 1.0$ and $R_{ground} = R_{main}$ using the first three steps outlined in the full ground effect methodology section . This figure shows that the boundary condition is satisfied at the center of the ground rotor; however, upward and downward flows are observed in different areas of the ground. Consequently, adjustments to the ground rotor size are needed and can be determined using the method detailed in the full ground effect methodology section .

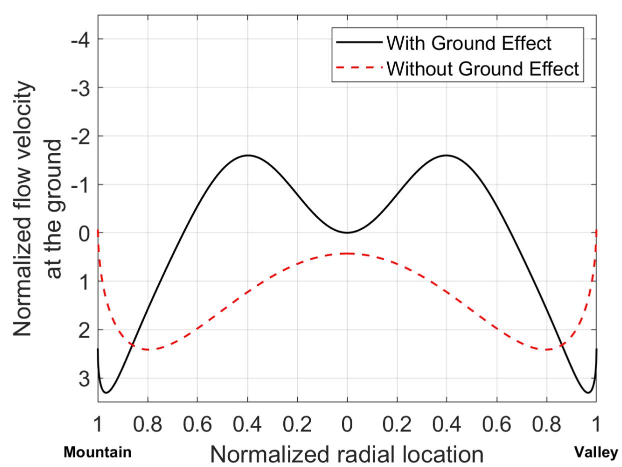

Figure 7: Wake velocity at the ground rotor for $H = R_{main}$, $R_{ground} = R_{main}$, and applying the first two steps in the full ground effect methodology.

Moreover, Figs. 8a and 8b show the variation of the standard relative error and error in percent within 40% of the rotor wake radius at the ground with the ground rotor factor (r_{factor}), respectively. This factor is the multiplier applied to the main rotor radius to determine the ground rotor radius. This figure illustrates that the ground rotor radius providing the lowest standard relative error differs from the one providing the lowest error in percent. Specifically, the ground rotor factors yielding the lowest standard relative error and the lowest error in percent are 2.37 and 2.3, respectively. The main goal of these two conditions is to ensure that the boundary condition at the ground is met and that the average rotor inflow in-ground effect is comparable to the Hayden formula. Thus, these error conditions are not enforced but serve as a guide for selecting the ground rotor radius that satisfies the boundary condition at the ground and produces results comparable to the Hayden formula. The red circle in these figures indicates that a ground rotor factor (r_{factor}) of 2.268 is needed to satisfy the boundary condition and achieve a result comparable to the Hayden formula for the $h = 1.0$ case.

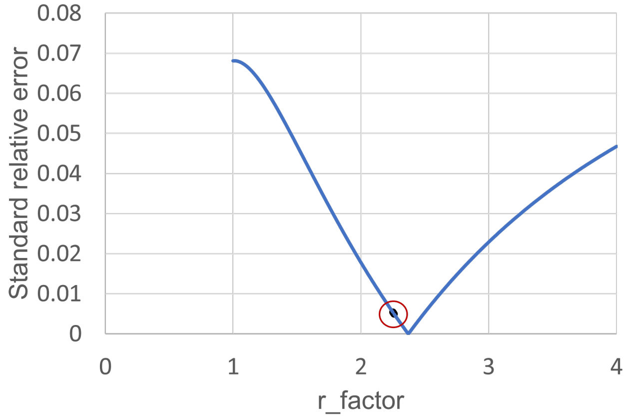

(a) Standard relative error variation with ground rotor factor

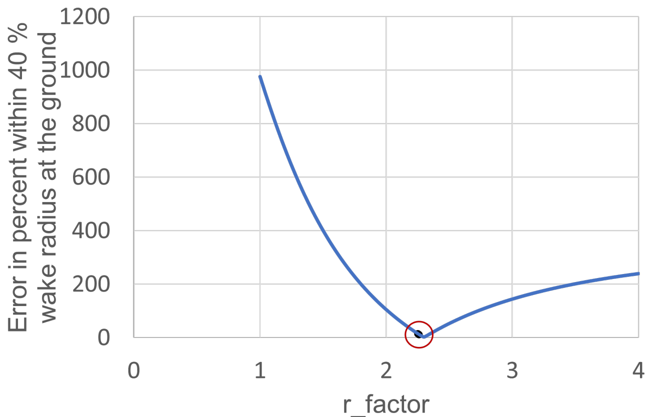

(b) Error in percent variation with ground rotor factor

Figure 8: Full ground effect errors variation with ground rotor factor (r_{factor}) where $R_{ground} = r_{factor}R_{main}$ for the R-50 rotor at H = R above the ground.

Additionally, Fig. 9a shows the wake velocity distribution versus the radial location at the rotor footprint on the ground surface for the case where $h = 1.0$ and $R_{ground} = 2.268R_{main}$. In this figure, the red-dashed curve represents the main rotor wake velocity at the ground plane. The solid black curve corresponds to the total flow velocity at the ground (boundary condition curve) after accounting for the effect of mass source distribution at the ground plane. This figure illustrates that the non-penetration flow boundary condition is satisfied across most of the wake footprint radius on the ground.

Furthermore, Fig. 9b displays three different curves. The blue-dashed curve represents the rotor inflow for the case with no ground effect. The red-dashed curve shows the upward flow created by the source distribution at the ground plane, located at $h = 1.0$ below the rotor. The black solid curve corresponds to the rotor inflow in-ground effect. This plot illustrates the reduction in the rotor inflow due to the presence of the ground.

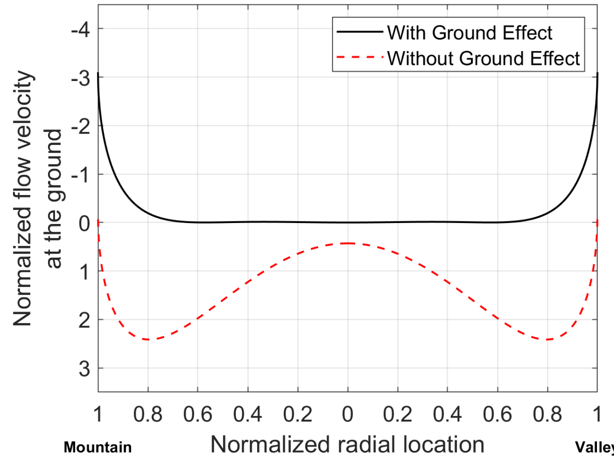

(a) Normalized Wake velocity distribution at the ground

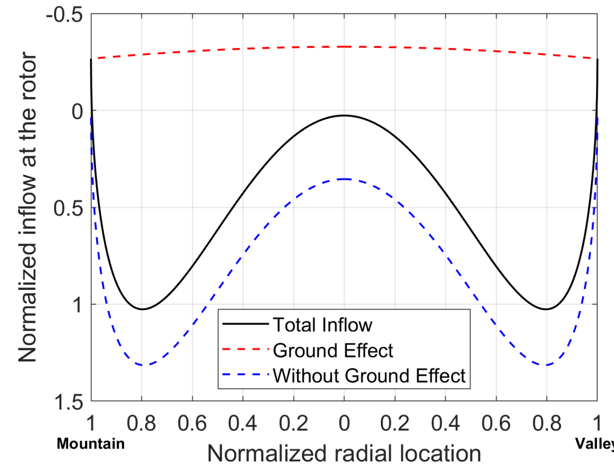

(b) Normalized rotor inflow distribution along radius

Figure 9: Full ground effect case for the R-50 rotor at H = R above the ground.

Full ground effect Correlations

Figure 10 compares the current approach with the Hayden model at various rotor heights above the ground. Additionally, Fig. 11 shows the standard relative error for these heights, indicating that most cases exhibit an error of approximately 0.003. Both Figs. 10 and 11 demonstrate that the current model correlates well with the Hayden model for all cases of rotor heights above ground greater than $0.5R_{main}$. The corresponding ground rotor radii needed to achieve these results are listed in Table 2, highlighting the importance of adjusting the ground rotor radius to satisfy the non-penetration flow boundary condition at the ground plane.

Moreover, Fig. 12 compares an isolated rotor inflow in ground effect between the current model and PPBFSM (Ref. 1) at various rotor heights above the ground. This figure illustrates that the current model exhibits a similar rotor inflow distribution trend compared to PPBFSM (Ref. 1) at various rotor heights above the ground. Additionally, the current model shows a greater rotor inflow reduction due to the presence

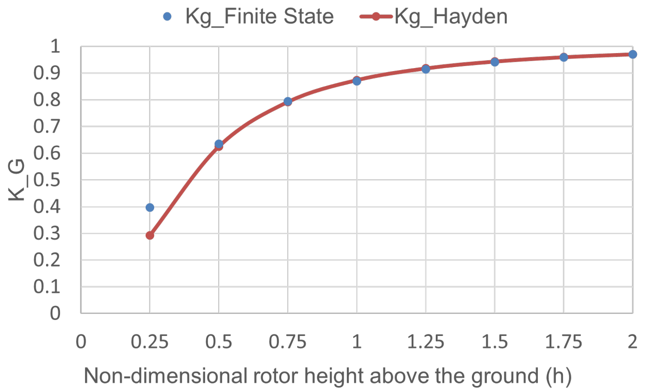

Figure 10: Comparison of the ground effect factor (K_G) at various non-dimensional rotor heights above the ground between the current finite state model and Hayden's model.

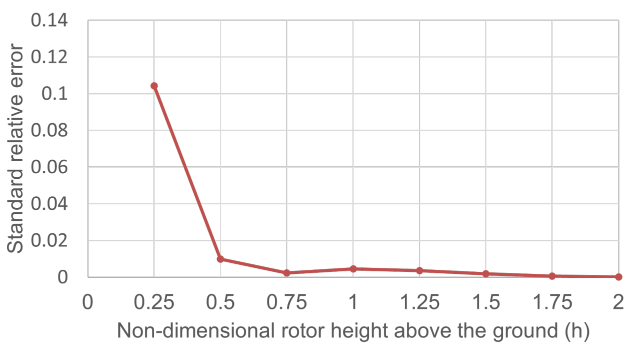

Figure 11: Standard relative error = $|k_{(G,FiniteState)} - K_{(G,Hayden)}|$ at various non-dimensional rotor heights above the ground.

of the ground at any given rotor height above the ground compared to PPBFSM. The difference between the two approaches arises from the fact that the current model explicitly imposes the non-penetration flow boundary condition at the ground rotor, whereas PPBFSM does not consider this boundary condition. Also, the current model is based on velocity potential, whereas PPBFSM relies on pressure potential.

Table 2: Ground rotor size (R_{ground}) for different non-dimensional rotor heights above ground (h).

h	R_{ground}
0.25	2.000 R_{main}
0.50	2.000 R_{main}
0.75	2.273 R_{main}
1.00	2.268 R_{main}
1.25	2.268 R_{main}
1.50	2.268 R_{main}
1.75	2.268 R_{main}
2.00	2.268 R_{main}

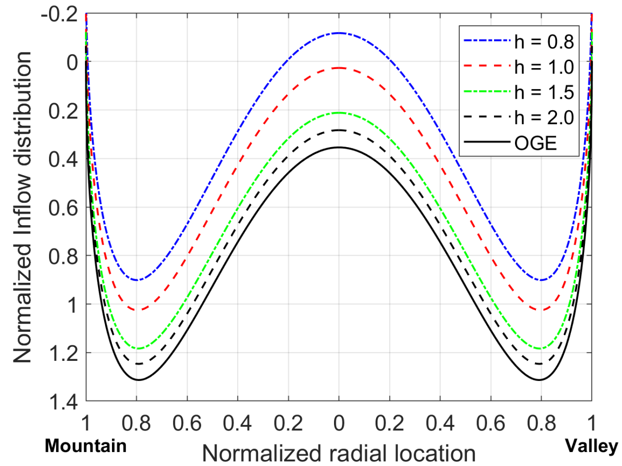

(a) Current velocity potential based finite state model

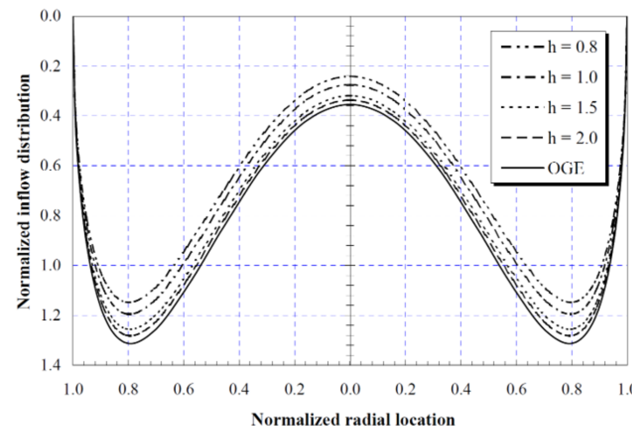

(b) Pressure potential based finite State model, (Ref. 1)

Figure 12: Comparison of normalized rotor inflow distribution for an isolated rotor between current VPBFSM and PPBFSM (Ref. 1) at various rotor heights above the ground in full ground effect.

Isolated Rotor in Inclined Ground Effect

The process outlined in the inclined ground effect methodology section is applied to study an isolated rotor above an inclined ground, using five zero-harmonics mass source distributions. Figure 13a shows the wake velocity distribution versus the radial location at the rotor footprint on the ground surface, in the ground frame of reference, for the case of $h = 0.9$, $R_{ground} = 2.268R_{main}$, and $\delta = 20°$. In this figure, the red-dashed curve corresponds to the main rotor wake velocity at the ground plane, and the solid black curve corresponds to the total flow velocity at the ground after including the effect of mass source distribution at the ground plane. This figure demonstrates that the non-penetration flow boundary condition is satisfied over most of the wake footprint radius at the ground plane.

Furthermore, Fig. 13b shows three different curves. The blue-dashed curve represents the rotor inflow with no ground effect. The red-dashed curve represents the upward flow created by the source distribution at the ground plane, located at $h = 0.9$ below the rotor with a 20° inclination angle. The black solid curve represents the rotor inflow in the presence of this inclined ground. This figure is shown in the main rotor frame of reference. Additionally, it shows a greater rotor inflow reduction on the mountain side than on the valley side, due to the inclined ground.

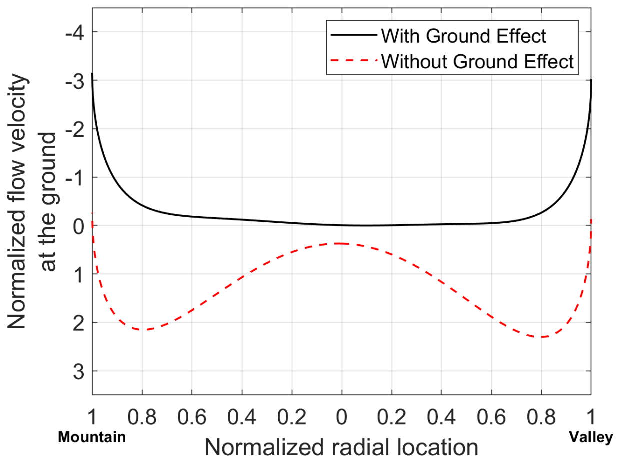

(a) Normalized Wake velocity distribution at the ground in the ground frame of reference

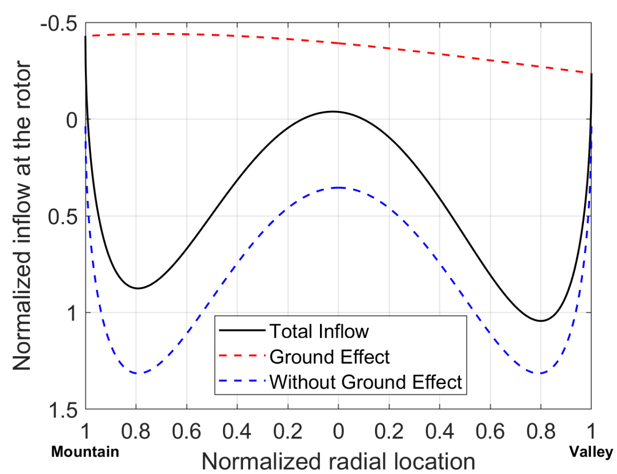

(b) Normalized rotor inflow distribution in the main rotor frame of reference

Figure 13: Inclined ground effect case for the R-50 rotor at H = 0.9 R above the ground with $\delta = 20°$.

Inclined ground effect Correlations

Figure 14 compares the rotor inflow distribution at a fixed height of $0.9R$ above the ground for various inclined ground angles between the current model and PPBFSM (Ref. 3). This figure illustrates that the current model exhibits a similar rotor inflow trend on the mountain side as PPBFSM, showing a greater reduction in rotor inflow as the ground inclination increases. However, on the valley side, the current model demonstrates a different rotor inflow distribution trend compared to PPBFSM. Specifically, as the ground inclination angle increases, the current model shows less reduction in the rotor inflow distribution on the valley side. In contrast, PPBFSM shows that the rotor inflow distribution on the valley side converges to the same result as without inclination, even at a high inclined ground angle of $\delta = 40°$. The difference in rotor inflow distribution between the two models, especially on the valley side, can be attributed to the current model imposing the non-penetration flow boundary condition at the ground, which is not considered in PPBFSM.

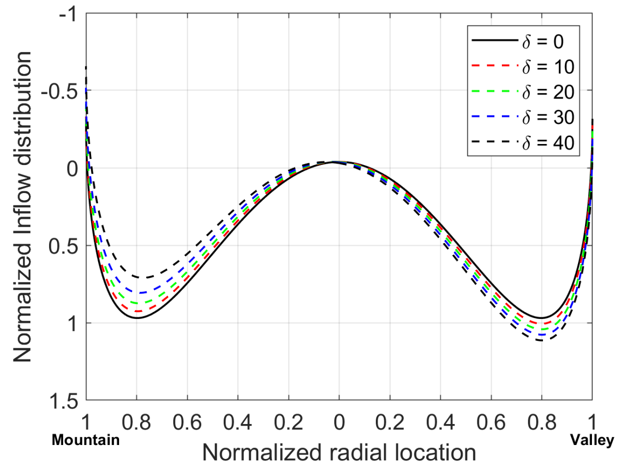

(a) Current velocity potential based finite state model

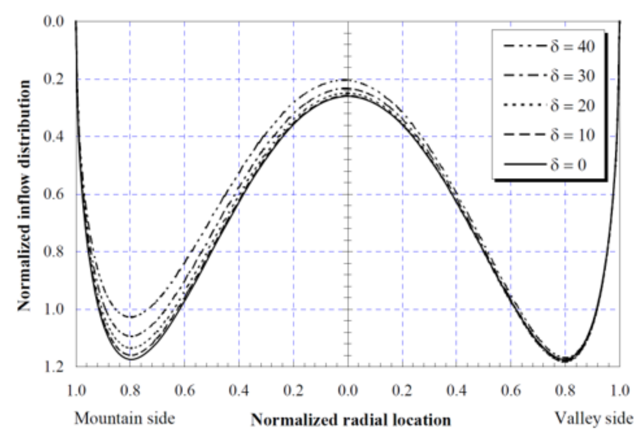

(b) Pressure potential based finite State model, (Ref. 3)

Figure 14: Comparison of normalized rotor inflow distribution for an isolated rotor between the current VPBFSM and PPBFSM (Ref. 3) at various ground inclination angles and $H = 0.9R_{main}$.

Theoretically, the valley side should experience less rotor inflow reduction as the ground inclination increases, a trend demonstrated by the current model but not by PPBFSM. This finding highlights the practical significance of incorporating the non-penetration flow boundary condition for more accurate predictions of rotor inflow in-ground effect.

Moreover, Fig. 15 compares the rotor inflow distribution at a fixed inclination ground angle of 25° for various rotor heights above the ground between the current model and PPBFSM (Ref. 3). This figure illustrates that the current model exhibits a similar inflow distribution trend as PPBFSM on both the mountain and valley sides. Additionally, the current model shows a greater reduction in rotor inflow distribution compared to PPBFSM, due to the imposition of the non-penetration flow boundary condition, which is considered in the current model but not in PPBFSM.

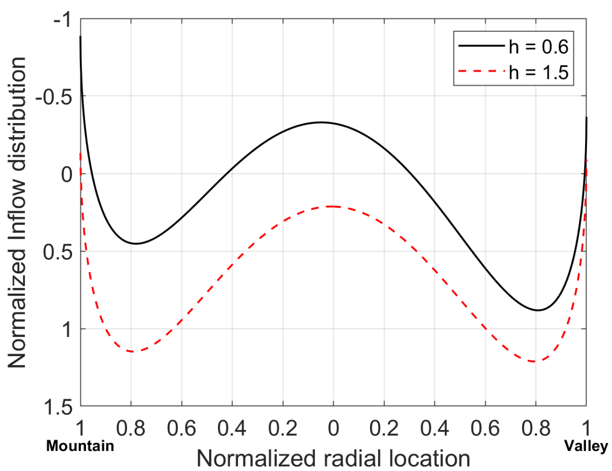

(a) Current velocity potential based finite state model

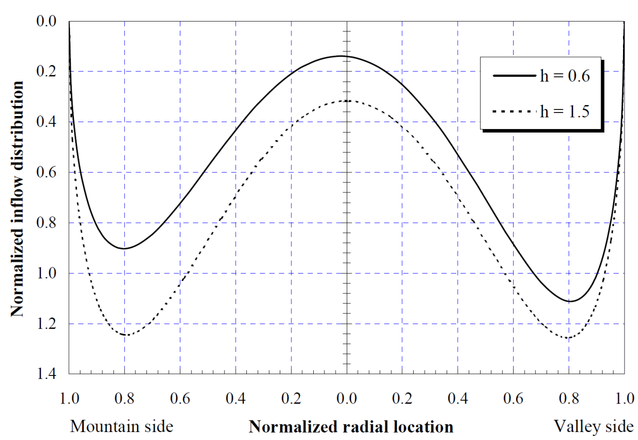

(b) Pressure potential based finite State model, (Ref. 3)

Figure 15: Comparison of normalized rotor inflow distribution for an isolated rotor between the current VPBFSM and PPBFSM (Ref. 3) at various rotor heights above the ground and $\delta = 25°$.

Isolated Rotor in partial Ground Effect

The process outlined in the partial ground effect methodology section is applied to study an isolated rotor above a partial ground rotor. Figure 16a shows the wake velocity distribution versus the radial location at the rotor footprint on the ground surface for the case where $h = 0.9$, $R_{ground} = 2.268 R_{main}$, and $d = 0$. In this case, the center of the main rotor is above the edge of the ground plane. In this figure, the red-dashed curve represents the main rotor wake velocity at the ground plane, and the solid black curve corresponds to the total flow velocity at the ground after accounting for the effect of mass source distribution at the ground plane. The vertical green dashed lines divide the plot into sections to illustrate the relative positions of the main rotor and the ground. The middle section indicates where the main rotor is directly above the ground, demonstrating that the boundary condition is met within the overlap region at the ground. The left section denotes where the main rotor is absent, while the right section shows where the ground rotor is absent.

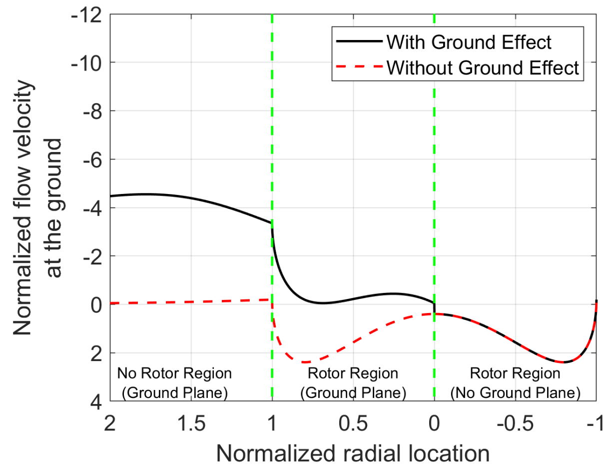

(a) Wake velocity distribution at the ground

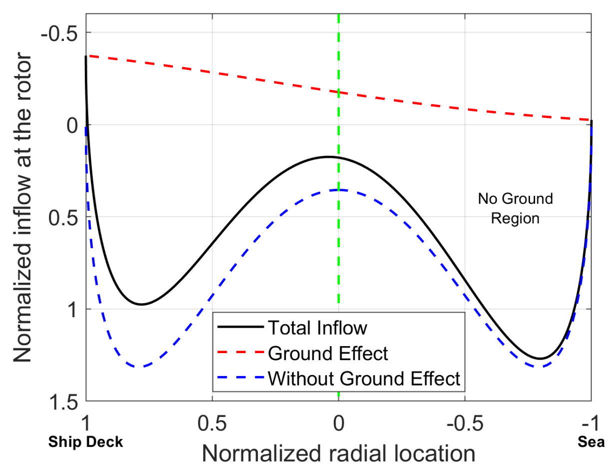

(b) Normalized rotor inflow distribution along radius

Figure 16: Partial ground effect case for the R-50 rotor at H = 0.9 R above the ground with $d = 0$.

Furthermore, Fig. 16b shows three different curves. The blue-dashed curve represents the rotor inflow without ground effect. The red-dashed curve represents the upward flow created by the source distribution at the ground plane, located at $h = 0.9$ below the rotor with a partial distance of $d = 0$. The solid black curve represents the total rotor inflow distribution in partial ground effect. This figure indicates a greater reduction in rotor inflow on the side where the ground is below the rotor (ship deck side) compared to the side with no ground below the rotor (sea side). The rotor inflow distribution in the partial ground effect behaves similarly to that in the inclined ground effect. For instance, the ship deck side in partial ground effect behaves like the mountain side in inclined ground effect.

Additionally, Fig. 17 shows the rotor inflow distribution in partial ground effect at a fixed partial distance of $d = 0$ for various rotor heights above the ground. This figure illustrates that as the rotor approaches the ground, there is a greater reduction in the inflow distribution on the ship deck side compared to the sea side. It also shows that on the sea side, the results are similar to the out-of-ground effect case, which is expected to occur theoretically in a real-life situation since there is no ground below the rotor.

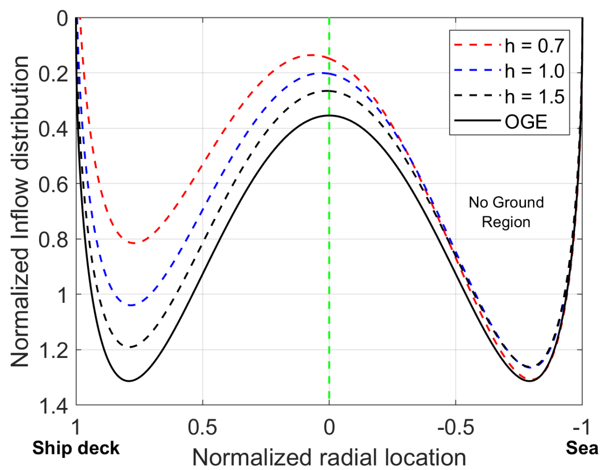

Figure 17: Partial ground effect case for the R-50 rotor at various rotor heights above the ground with $d = 0$.

Partial ground effect Correlations

Figure 18 compares an isolated rotor at a fixed height of $0.9R$ above the ground for various partial ground distances between the current model and PPBFSM (Ref. 3). In this figure, the current model shows a noticeable difference in rotor inflow distribution trend compared to PPBFSM. On the ship deck side, the current model shows that the rotor inflow distribution closely resembles the full-ground effect case for this rotor height above the ground, as expected to occur theoretically in a real-life situation. In contrast, PPBFSM displays results that significantly deviate from the full-ground effect case for this side of the main rotor. On the sea side, the rotor inflow distribution in the current model aligns closely with the out-of-ground effect result, which is also expected in a real-life situation. However, PPBFSM shows a reduction in the rotor inflow distribution on the sea side. These differences in rotor inflow between the current model and PPBFSM arise from the imposition of the flow boundary condition in the current model, which is not considered in PPBFSM.

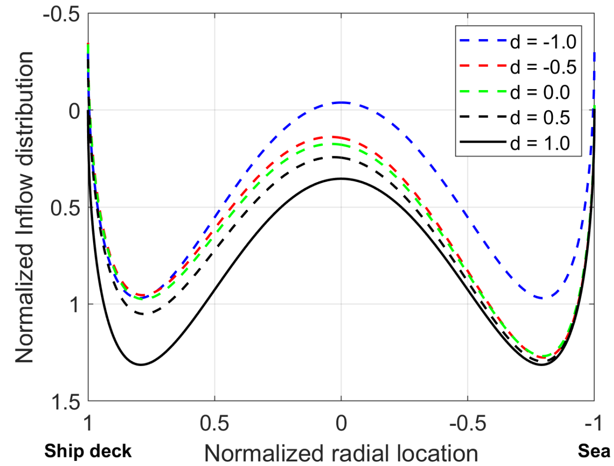

(a) Current velocity potential based finite state model

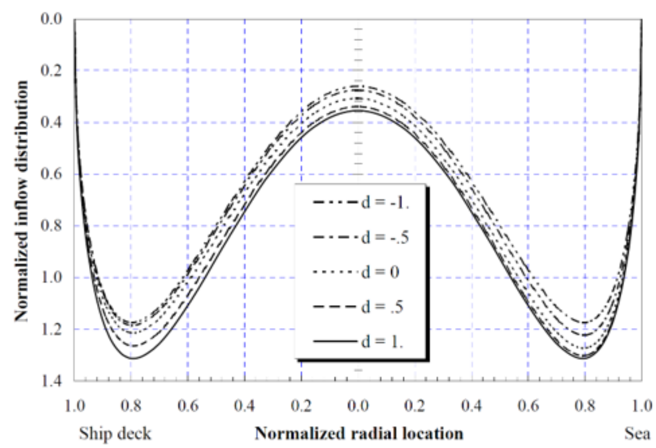

(b) Pressure potential based finite State model, (Ref. 3)

Figure 18: Comparison of normalized rotor inflow distribution for an isolated rotor between the current VPBFSM and PPBFSM (Ref. 3) at $H = 0.9R_{main}$ and various partial distances of ground.

CONCLUSIONS

A new approach has been developed using the Velocity Potential Based Finite State Model (VPBFSM) to enforce the non-penetration flow boundary condition at the ground. It studies an isolated rotor in normal, inclined, and partial ground effect cases. The main and ground rotors are represented as load and mass source distributions in the flow field, respectively. Additionally, an equation has been formulated to determine the mass source distributions of the ground rotor in terms of the main rotor loading for imposing the non-penetration flow boundary condition. However, the boundary condition is not enforced due to the exclusion of the $n = m$ terms in computing the ground flow velocities, which according to the literature including these terms, would introduce infinite kinetic energy into the flow field. Therefore, adjustments to the estimated strengths of the mass source distributions and the size of the ground rotor are necessary to impose the boundary condition at the ground. Methods have been developed to adjust these estimated strengths and ground rotor size for full, inclined, and partial ground effect cases. The study focuses on the R-50 unmanned helicopter rotor, analyzing its behavior in these different ground effect cases. The full ground effect results are compared with the Hayden model and the Pressure Potential Finite State Model (PPBFSM). The inclined and partial ground effect results are correlated with PPBFSM. The following conclusions are drawn from this study:

1. The average rotor inflow velocity of the current model has been compared with the Hayden model across various rotor heights above the ground. This comparison demonstrates that the current model correlates well with the Hayden model for all rotor heights greater than $0.5R_{main}$, with an error of 0.003 for most cases.

2. The rotor inflow distribution in normal ground effect shows a trend similar to the Pressure Potential-Based Finite State Model (PPBFSM) for an isolated rotor at various heights above the ground. Additionally, the current model demonstrates a greater reduction in rotor inflow distribution due to ground presence than PPBFSM. This difference stems from the enforcement of the non-penetration flow boundary condition at the ground in the current approach, which is not considered in PPBFSM.

3. In the inclined ground effect case, the rotor inflow distribution is studied for a fixed height of $0.9R$ above the ground across various ground inclination angles. The current model demonstrates a distinct and plausible trend compared to PPBFSM. Specifically, on the valley side, the current approach shows less reduction in rotor inflow as the ground inclination angle increases, which aligns with theoretical expectations for real-life situations. In contrast, PPBFSM does not exhibit this behavior. This difference can be attributed to the current model imposing the boundary condition at the ground, whereas PPBFSM does not consider this boundary condition.

4. At different rotor heights above a 25° inclined ground angle, the current approach shows a similar rotor inflow distirbution trend as PPBFSM. Also, the current approach exhibits more rotor inflow reduction on both sides of the rotor compared to PPBFSM. This is because the current approaches experience more ground effect as the rotor approaches the ground compared to the PPBFSM

5. In the partial ground effect case, the current approach demonstrates a more reasonable rotor inflow distribution trend compared to PPBFSM for various partial ground distances (d) and a fixed rotor height above the ground ($h = 0.9$). On the ship deck side, the current approach shows a reduction in rotor inflow comparable to full ground effect conditions, as expected in a real-life situation. In contrast, PPBFSM does not exhibit this behavior. On the sea side, where there is no ground presence, the current approach shows results comparable to the out-of-ground effect case, which is also expected to be in a real-life situation. However, PPBFSM does not reflect this behavior. These differences arise because the current model imposes the boundary condition at the ground, whereas PPBFSM does not account for this boundary condition.

Finally, the current model shows a good representation of an isolated rotor inflow distribution reduction in normal, inclined, and partial ground effect cases, as would be expected in real-life situations in these cases. In this approach, the equation developed to compute the strengths of the mass source distribution in terms of rotor loading revealed that the boundary condition at the ground is not adequately enforced, primarily due to the exclusion of $n = m$ terms in computing the ground flow velocities. Consequently, adjustments were made to the ground rotor size and the estimated strengths of the mass source distribution. Future studies are needed to investigate the inclusion of $n = m$ terms in computing the ground flow velocities, aiming to eliminate the need for adjustments to the ground rotor size when enforcing the boundary condition.

Authors contact:
Andro Metry ametry3@gatech.edu
J.V.R. Prasad jvr.prasad@ae.gatech.edu
D.A. Peters dap@wustl.edu

APPENDIX A

ELLIPSOIDAL COORDINATE SYSTEM

The ellipsoidal coordinate system (ν, η, ψ) is defined as:

$$\bar{x} = -\sqrt{1-\nu^2}\sqrt{1+\nu^2}cos(\psi) \tag{16}$$

$$\bar{y} = \sqrt{1-\nu^2}\sqrt{1+\nu^2}sin(\psi) \tag{17}$$

$$\bar{z} = -\nu\eta \tag{18}$$

where $\bar{x}, \bar{y}, \bar{z}$ are the Cartesian coordinates normalized by the rotor radius. The values of ν, η, ψ cover entire 3-dimensional space if they are restricted to the following ranges:

$$-1 \leq \nu \leq 1 \tag{19}$$

$$0 \leq \eta \leq \infty \tag{20}$$

$$0 \leq \psi \leq 2\pi \tag{21}$$

Figure 19 shows the ellipsoidal coordinate system viewed in the $\bar{x} - \bar{z}$ plane. While ν defines constant hyperboloid surfaces, ν defines constant ellipsoid surfaces. Both families of surfaces are azimuthally symmetric about the $\bar{z} - axis$. When $\eta = 0$, surfaces represent two faces of the disk, and ν changes sign across the disk. The inverse of Eqs.(16) through (18) is given as:

$$\nu = -\frac{sign(\bar{z})}{\sqrt{2}}\sqrt{(1-\bar{S}) + \sqrt{(1-\bar{S}) + 4\bar{z}^2}} \tag{22}$$

$$\eta = \frac{1}{\sqrt{2}}\sqrt{(\bar{S}-1)+\sqrt{(\bar{S}-1)+4\bar{z}^2}} \tag{23}$$

$$\psi = tan^{-1}(\frac{-\bar{y}}{\bar{x}}) \tag{24}$$

where

$$\bar{S} = \bar{x}^2+\bar{y}^2+\bar{z}^2 \tag{25}$$

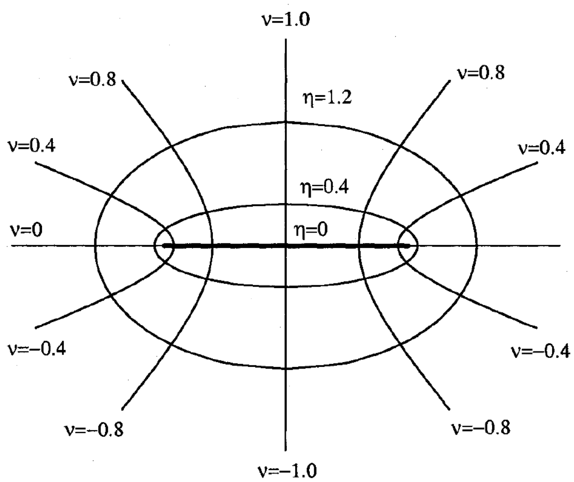

Figure 19: Ellipsoidal coordinate system.

APPENDIX B

NORMALIZED ASSOCIATED LEGENDRE FUNCTIONS

$\bar{P}_n^m(\nu)$ and $\bar{Q}_n^m(i\eta)$ are normalized associated Legendre functions of the first and second kind, respectively (Refs. 17, 18).

$$\bar{P}_n^m = (-1)^m \frac{P_n^m(\nu)}{\rho_n^m(\nu)} \tag{26}$$

$$\bar{Q}_n^m = (-1)^m \frac{Q_n^m(i\eta)}{Q_n^m(i0)} \tag{27}$$

$$(\rho_n^m)^2 = \int_0^1 [P_n^m(\nu)]^2 d\nu = \frac{1}{2n+1}\frac{(n+m)!}{(n-m)!} \tag{28}$$

$$Q_n^m(i0) = \begin{cases} -\frac{\pi}{2}(i)^{n+1}\frac{(n+m-1)!!}{(n-m)!!} & n+m = even \\ (i)^{n+1}\frac{(n+m-1)!!}{(n-m)!!} & n+m = odd \end{cases} \tag{29}$$

APPENDIX C

AXIAL INDUCED VELOCITY COMPONENT

A review of deriving an equation to compute the velocity on and above the rotor disk is presented in this section and a detailed derivation is discussed in Ref.(6). In general, the velocity can be represented as a gradient of the velocity potential:

$$\vec{v} = \vec{\nabla}\Psi \tag{30}$$

where $\vec{v}$ is the velocity vector, Ψ is the velocity potential.

The velocity potential consists of time and spatial-dependent parts, i.e., velocity potential states (a_n^m) for time dependency and shaping function $(\tilde{\Psi}_n^m)$ for spatial dependency. Thus, Eq. (30) can be rewritten for cosine term as follows:

$$\vec{v} = \sum_{m=0}^{\infty}\sum_{n=m+1}^{\infty}(a_n^m \vec{\nabla}\tilde{\Psi}_n^{mc}) \tag{31}$$

where

$$\tilde{\Psi}_n^{mc} = \sigma_n^m \Phi_{n+1}^{mc} + \zeta_n^m \Phi_{n-1}^{mc} \tag{32}$$

σ , and ζ are constants and defined in Ref.(6). Φ is the pressure potential (shaping function) and is defined as follows:

$$\Phi_n^{mc} = \bar{P}_n^m(\nu)\bar{Q}_n^m(i\eta)cos(m\bar{\psi}) \tag{33}$$

After conducting the gradient of the Eq.(32) in the axial direction:

$$\frac{\partial\tilde{\Psi}_n^{mc}}{\partial z} = \frac{\partial(\sigma_n^m\Phi_{n+1}^{mc}+\zeta_n^m\Phi_{n-1}^{mc})}{\partial z} = \Phi_n^{mc} \quad , where\ n > m \tag{34}$$

The velocity on and above the rotor disk can be calculated using the velocity potential state and the shaping function which can be defined as follows:

$$\vec{v}_z = \sum_{m=0}^{\infty}\sum_{n=m+1}^{\infty} a_n^m \frac{\partial\tilde{\Psi}_n^{mc}}{\partial z} = \sum_{m=0}^{\infty}\sum_{n=m+1}^{\infty} a_n^m \Phi_n^{mc} \tag{35}$$

APPENDIX D

CORRELATION MATRIX FOR GROUND EFFECT

Each rotor has two types of velocity, one is the self-flow velocity of the rotor and the other is the effect of one rotor on the other rotor.

The self-flow velocity of the main rotor and ground can be computed using the following equation:

$$\vec{v}_{SelfRotor} = \sum_{m=0}^{\infty}\sum_{n}^{\infty} a_n^m \Phi_n^{mc} \tag{36}$$

The difference between the self-flow velocity of the ground and the main rotors is the radial distribution (n). For the self-flow velocity of the main rotor, $n = m+1, m+3$ while the self-flow velocity of the ground rotor $n = m+2, m+4$. Also, to differentiate between the velocity states of the main rotor and ground rotor, let a_n^m be c_j^r for the ground rotor.

Moreover, Fig. 1 shows the coordinate system that can be used to compute any points below the rotor within the wake radius, Ref. (15), and also described as follows:

$$\vec{v}_A = \vec{v}_B + \vec{v}_C^* - \vec{v}_D^* \tag{37}$$

where induced velocity at point A ($\vec{v}_A$) is the wake velocity at ground ($\vec{v}_{MainOnGround}$), point B ($\vec{v}_B$) is induced velocity on the disk, points C ($\vec{v}_C^*$) is adjoint induced velocity on the disk and D ($\vec{v}_D^*$) is adjoint induced velocity above the disk.

Also, Equation (37) can be simplified as $\vec{v}_c^*$ and $\vec{v}_D^*$ are independent of time changes due to the steady state assumption and this leads to the following equation:

$$\vec{v}_A = 2\vec{v}_B - \vec{v}_D \tag{38}$$

For steady state, the strengths of the mass source distributions at the ground rotor can be estimated by equating the flow velocity exerted by main rotor on the ground to the exit flow velocity of the mass source distributions at the ground:

$$\vec{v}_{MainOnGround} = \vec{v}_{SelfGround} \tag{39}$$

where $\vec{v}_{MainOnGround}$ and $\vec{v}_{SelfGround}$ can be expressed as follows:

$$\vec{v}_{MainOnGround} = \sum_{m=0}^{\infty} \sum_{n=m+1}^{\infty} a_n^m (2\Phi_n^{mc}|_{SelfRotor} - \Phi_n^{mc}|_{AboveRotor}) \tag{40}$$

$$\vec{v}_{SelfGround} = \sum_{r=0}^{\infty} \sum_{j=r+2}^{\infty} c_j^r \Phi_j^{rc}|_{SelfGround} \tag{41}$$

After substituting Eq. (40) and Eq. (41) in Eq. (39) and applying the orthogonality properties of the normalized associated Legendre function, a general relation between velocity states of the ground and the main rotor can be found and expressed as follows:

$$c_j^r = [G_{jn}^{rm}] a_n^m \tag{42}$$

$$r = 0,1 \quad j = r+2, r+4 \quad m = 0,1 \quad n = m+1, m+3$$

where G is the correlation matrix and it is defined as follows:

$$G_{jn}^{rm} = 2\int_0^1 \bar{P}_j^r(\nu_2)\bar{P}_n^m(\nu_1) d\nu_2 - \int_0^1 \bar{P}_j^r(\nu_2)\bar{P}_n^m(\nu_1)\bar{Q}_n^m(\eta_1) d\nu_2 \tag{43}$$

where $\bar{P}$ and $\bar{Q}$ are the normalized associated Legendre function first and second kind, respectively; the subscripts 1 and 2 correspond to the data of the main rotor and the ground rotor, respectively. It is recommended to use the trapezoidal rule to solve the integration of this equation as the variable ν may not be equidistant.

Finally, for steady state, the strengths of the mass source distributions at the ground can be related to the load distribution at the main rotor using the relation between velocity potential states and pressure terms, and it is as follows:

$$\begin{Bmatrix} \tau_n^m = [V_L]_{rotor}\ a_n^m \\ \omega_j^r = [V_L]_{ground}\ c_j^r \end{Bmatrix} \tag{44}$$

where τ and ω are pressure coefficients corresponding to load distribution (main rotor) and mass source distribution (ground rotor), respectively. $[V_L]_{rotor}$, $[V_L]_{ground}$ are the mass flow parameters for the main rotor and ground rotor, respectively. The mass flow parameter for the ground is defined as diagonal matrix with twice the average of main rotor velocity out-of-ground at the diagonal. The mass flow parameter for the main rotor is defined the same as the ground rotor except the first element in the matrix is only the average of the main rotor velocity out-of-ground effect which corresponds to a_1^0.

A direct relationship between the strengths of the mass source distributions at the ground rotor and the load distributions at the main rotor can be obtained by substituting Eq. (44) in Eq. (42), and it is as follows:

$$\omega_j^r = [S_{jn}^{rm}]\tau_n^m$$

$$r = 0,1 \quad j = r+2, r+4 \quad m = 0,1 \quad n = m+1, m+3 \tag{45}$$

where $[S_{jn}^m]$ is a correlation matrix and it is defined as follows:

$$[S_{jn}^{rm}] = [V_e][G_{jn}^{rm}]$$

$$r = 0,1 \quad j = r+2, r+4 \quad m = 0,1 \quad n = m+1, m+3 \tag{46}$$

$$V_e = \begin{bmatrix} 2 & & & 0 \\ & 1 & & \\ & & \ddots & \\ 0 & & & 1 \end{bmatrix} \tag{47}$$

Since in this paper, even pressure coefficients and velocity potential states are used for the ground rotor finite state equation so the first element in the mass flow matrix is twice the average velocity of the main rotor out-of-ground effect. However, if odd velocity potential states are used including c_1^0 then V_e will be an identity matrix.

The general form of expressing the strengths of the mass source distributions in terms of rotor loading is as follows:

$$\begin{aligned} \omega_j^{0c} &= \frac{1}{2\pi} \sum_{m=0}^{\infty} \sum_{n=m+1}^{\infty} \int_0^{2\pi} S_{jn}^{rm}(\tau_n^{mc} cos m\bar{\psi}_1 + \tau_n^{ms} sin m\bar{\psi}_1) cos r\bar{\psi}_2 d\bar{\psi}_2 \\ \omega_j^{rc} &= \frac{1}{\pi} \sum_{m=0}^{\infty} \sum_{n=m+1}^{\infty} \int_0^{2\pi} S_{jn}^{rm}(\tau_n^{mc} cos m\bar{\psi}_1 + \tau_n^{ms} sin m\bar{\psi}_1) cos r\bar{\psi}_2 d\bar{\psi}_2 \\ \omega_j^{rs} &= \frac{1}{\pi} \sum_{m=0}^{\infty} \sum_{n=m+1}^{\infty} \int_0^{2\pi} S_{jn}^{rm}(\tau_n^{mc} cos m\bar{\psi}_1 + \tau_n^{ms} sin m\bar{\psi}_1) sin r\bar{\psi}_2 d\bar{\psi}_2 \end{aligned} \tag{48}$$

ACKNOWLEDGMENTS

This research was partially funded by the U.S. Government under Cooperative Agreement No. W911W6-21-2-0001. The U.S. Government is authorized to reproduce and distribute reprints for Government purposes notwithstanding any copyright notation thereon.

The views and conclusions contained in this document are those of the authors and should not be interpreted as representing the official policies of position, either expressed or implied, of the U.S. Army Combat Capabilities Development Command (DEVCOM), Aviation & Missile Center (AvMC), or the U.S. Government.

REFERENCES

1. Xin, H., Prasad, J. V. R., and Peters, D. A., "Dynamic Inflow Modeling for Simulation of a Helicopter Operating in Ground Effect," Proceedings of AIAA Modeling and Simulation Technology Conference, Paper No. AIAA-99-4114, August 1999.

2. Xin, H., Prasad, J. V. R., and Peters, D. A., "Inflow Modeling for Simulation of Helicopter Flight in Dynamic Ground Effect," Proceedings of the 25th European Rotorcraft Forum, September 1999.

3. Xin, H., *Development and validation of a generalized ground effect model for lifting rotors*, Georgia Institute of Technology, 1999.

4. Zhang, H., Prasad, J. V. R., and Peters, D. A., "Finite State in-Ground Effect Inflow Models for Lifting Rotors," American Helicopter Society 52nd Annual Forum Proceedings, Vol. 2, June 1996.

5. Zhang, H., Prasad, J. V. R., and Peters, D. A., "Finite State Inflow Models for Lifting Rotors in Ground Effect," American Helicopter Society 53rd Annual Forum Proceedings, Vol. 2, April 1997.

6. Morillo, J. A., and Peters, D. A., "Velocity Field Above a Rotor Disk by a New Dynamic Inflow Model," *Journal of Aircraft*, Vol. 39, (5), 2002, pp. 731–738.

7. Peters, D. A., Morillo, J. A., and Nelson, A. M., "New Developments in Dynamic Wake Modeling for Dynamics Applications," *Journal of the American Helicopter Society*, Vol. 48, (2), April 2003, pp. 120–127.

8. Yu, K., and Peters, D. A., "Net Mass Flow Components in a Three-Dimensional Unsteady Rotor Inflow Model," Proceedings of the International Mechanical Engineering Congress and Exposition 2003, Paper No. IMECE2003-42459, November 2003.

9. Yu, K., and Peters, D. A., "Use of Potential Flow State-Space Inflow Modeling for Mass Source Rotors," *The Aeronautical Journal*, Vol. 108, (1085), July 2004, pp. 333–344.

10. Yu, K., and Peters, D. A., "Nonlinear State-Space Modeling of Ground Effect," *Journal of the American Helicopter Society*, Vol. 50, (30), July 2004, pp. 333–344.

11. Metry, A., Prasad, J. V. R., and Peters, D. A., "Finite State Modeling of Ground Effect Using Mass Source Distribution at the Ground Plane," Proceedings of the 80th Vertical Flight Society Forum, May 2024.

12. Guner, F., Prasad, J. V. R., and Peters, D. A., "An Approximate Finite State Dynamic Wake Model for Below the Rotor Inflow Predictions," *Journal of the American Helicopter Society*, Vol. 66, (3), July 2021, pp. 1–10. DOI: 10.4050/JAHS.66.032007

13. Guner, F., Prasad, J. V. R., He, C., and Peters, D. A., "Fidelity Enhancement of a Multi-Rotor Dynamic Inflow Model via System Identification," *Journal of the American Helicopter Society*, Vol. 67, (2), April 2022, pp. 1–17. DOI: 10.4050/JAHS.67.022009

14. He, C., *Development and Application of a Generalized Dynamic Wake Theory for Lifting Rotors*, Ph.D. thesis, Georgia Institute of Technology, July 1989.

15. Fei, Z., *A Rigorous Solution for Finite-State Inflow Throughout the Flowfield*, Ph.D. thesis, Washington University in St. Louis, May 2013.

16. Hayden, J. S., "The Effect of the Ground on Helicopter Hovering Power Required," Proc. AHS 32nd Annual Forum, 1976.

17. Gradshteyn, I. S., and Ryzhik, I. M., *Table of Integrals, Series, and Products*, Academic Press, New York, 1980, pp. 948–965.

18. Abramowitz, M., and Stegun, I. A., *Handbook of Mathematical Functions*, Academic Press, New York, 1970, pp. 332–341.